Applied Thermal Engineering 288 (2026) 129563

Contents lists available at ScienceDirect

Applied Thermal Engineering

journal homepage: www.elsevier.com/locate/ate

Research Paper

Passive thermal management of a Li-ion battery module using phase change materials

Arijeet Paul Avik [a], Arunachala Mada Kannan [b,a], Vesa Ruuskanen [a], Soroush Mostafaie [a], Pertti Kauranen [a,*]

[a] Lappeenranta-Lahti University of Technology LUT, P.O. Box 20, FI-53851, Lappeenranta, Finland
[b] Ira A. Fulton Schools of Engineering, ISTB3 #109, Arizona State University, 7418 E. Innovation Way South, Mesa, AZ 85212, United States of America

ARTICLE INFO

Keywords:
Phase change material
Thermal management
Li-ion battery
Charge–discharge cycling
Temperature

ABSTRACT

This study evaluates the feasibility of a passive phase change material (PCM)-based battery thermal management system intended for use in non-road mobile machines (NRMM). Two 3P4S modules, each with a nominal energy of 200 W h, were assembled from high-power cylindrical NCA Li-ion cells: one module was filled with a commercial paraffin PCM and the other was a reference without PCM. The modules were cycled at 1C, 1.5C, and 2C under identical ambient conditions, and module temperatures were recorded during charge and discharge. The results show that the PCM exhibits distinct thermal behavior at different C-rates. At 1C, the sensible heat of the solid PCM is sufficient to limit the temperature rise of the module. At 1.5C, the module temperature reaches the PCM melting point and remains approximately constant. At 2C, practically all PCM melts, which delays the temperature rise but its effect is constrained by the poor thermal conductivity of the organic PCM. The added PCM mass reduced the module gravimetric energy density from 231 $W\,h\,kg^{-1}$ to 146 $W\,h\,kg^{-1}$. Nevertheless, the results indicate that paraffin-based passive PCM thermal management can effectively limit temperature rise and improve the thermal behavior of high-power NCA battery modules at moderate C-rates, while still maintaining a competitive system-level energy density for small-scale applications.

1. Introduction

The demand for lithium-ion batteries (LIBs) continues to rise across a wide spectrum of applications, from portable electronic devices to electric vehicles (EVs). Owing to their high energy density, long cycle life, absence of memory effect, and low self-discharge rates, LIBs have become the benchmark technology in modern energy storage [1,2]. In addition to on-road EVs, the electrification of non-road mobile machinery (NRMM) with Li-ion batteries is considered a promising means of reducing greenhouse gas emissions [3]. For smaller NRMM platforms, such as compact city tractors, passive battery thermal management solutions are particularly attractive because they can provide adequate temperature control without the added complexity and cost of liquid-cooled systems.

Based on positive electrode (cathode) chemistry, LIBs are commonly categorized into nickel manganese cobalt oxide (NMC), lithium iron phosphate (LFP), and nickel cobalt aluminum oxide (NCA), with NMC and NCA dominating electric mobility applications. Commercial EV manufacturers primarily deploy NMC 532 and NMC 622 chemistries [4], but there is an accelerating transition toward NMC 811 batteries, which deliver higher energy density, reduced weight, extended driving ranges, and decreased cobalt dependency, thereby enhancing sustainability and cost-effectiveness in the EV sector [5]. Tesla represents a unique case as the only EV producer employing NCA chemistry, asserting that its NCA cells incorporate a lower cobalt fraction relative to NMC 811 batteries [6,7].

The thermal sensitivity of LIBs originates from their electrochemical processes, which are intrinsically temperature-dependent. Heat generation in LIBs is governed by several internal mechanisms, including Joule heating, polarization heating, and decomposition heating [8,9]. The extent of this thermal generation is further influenced by aging [10], ambient temperature [1], and electrolyte properties [1,11]. Elevated temperatures accelerate parasitic reactions, causing electrode degradation, reduced cycle life and power density, capacity fade, and an increased probability of thermal runaway [9,12,13]. At low temperatures, ionic transport is hindered, capacity is diminished, and lithium plating becomes more pronounced, posing significant safety risks [13,14]. Temperature non-uniformities, often arising from manufacturing inconsistencies, can induce localized hot spots, increase internal resistance, accelerate aging, and heighten the requirement for charge

* Corresponding author.
E-mail address: pertti.kauranen@lut.fi (P. Kauranen).

https://doi.org/10.1016/j.applthermaleng.2025.129563
Received 2 October 2025; Received in revised form 1 December 2025; Accepted 17 December 2025
Available online 24 December 2025

Nomenclature

Variables

ΔH	Latent heat
C	Heat Capacity
Q	Thermal Energy

Subscripts and Superscripts

amb	Ambient
bat	Battery
el	Electrical
G	Gamry
int	Internal
irr	Irreversible
lat	Latent
m	Melting
rev	Reversible
s	Solidification
sens	Sensible

Acronyms

ARC	Accelerated Rate Calorimeter
BEV	Battery Electric Vehicle
BTMS	Battery Thermal Management Systems
CA	Capric Acid
CC	Constant Current
CV	Constant Voltage
DSC	Differential Scanning Calorimetry
EG	Extended Graphite
EV	Electric Vehicle
HP	Heat Pipe
IR	Infrared
LA	Lauric Acid
LFP	Lithium Iron Phosphate
LIB	Lithium-ion Battery
NCA	Nickel Cobalt Aluminum Oxide
NMC	Nickel Manganese Cobalt Oxide
NRMM	Non-Road Mobile Machinery
PA	Paraffin
PCM	Phase Change Material
PHEV	Plug-in Hybrid Electric Vehicle
RT	Rubitherm
RTD	Resistance Temperature Detector
SOC	State Of Charge

balancing between cells [12,15]. The optimal operating temperature for LIBs lies within 20 to 40 °C and should not exceed 50 °C [1,13,16]. For NCA-based cells, the safe operational window typically spans −20 to 60 °C during discharge and 0 to 45 °C during charge [17]. Deviations from these ranges result in performance degradation, energy inefficiency, and elevated safety hazards such as thermal runaway [1].

To mitigate these challenges, Battery Thermal Management Systems (BTMS) are essential to maintain the battery temperature within a safe and optimal range. They are typically classified as active, passive, or hybrid, depending on their reliance on external energy [1]. Active systems employ fans or pumps to circulate air or liquid, effectively dissipating heat but reducing the driving range of electric vehicles due to additional energy demand [1,12]. On the other hand, passive systems rely on materials such as Phase Change Materials (PCMs), which absorb and release heat during phase transitions, naturally regulating cell temperature and improving uniformity without external power [16]. Hybrid BTMS integrate both approaches. Among these, PCMs have attracted significant interest for their energy efficiency, compactness, cooling capacity, low maintenance, and ability to maintain battery temperature uniformity and operational ranges [1,15,18,19]. Effective PCMs for BTMS require high latent heat and specific heat capacity, good thermal conductivity, phase change temperatures aligned with LIB operating windows, minimal volume change, and favorable stability and safety characteristics [1,15,16,19–21]. According to Rao et al. [22], the melting point is the key selection criterion, with optimal performance achieved below 45 °C, consistent with Zhao et al. [13], who reported the optimal LIB operating range as 20–50 °C.

PCM-based BTMS research has mainly focused on single-cell configurations, testing a range of PCM materials with individual LIB cells. Weng et al. [23] examined paraffin-based PCMs with melting points of 35 °C, 42 °C, and 55 °C for 18650 NMC cells, while Srivastava et al. [24] evaluated Eicosane, commercial RT42 paraffin, and Capric acid, finding that Eicosane yielded the lowest peak temperature of 40 °C at 3C discharge.

To enhance thermal conductivity, researchers have incorporated additives or fins into pure PCMs. Bais et al. [25] used commercial RT42 paraffin with Al_2O_3 nanoparticles at 3C discharge, reporting peak temperatures between 45.24 and 52.67 °C. Rajan et al. [26] employed copper foam-enhanced 1-tetradecanol in an LFP cell, reducing peak temperatures from 49.5 to 43 °C at 2C. Wu et al. [27] developed paraffin/OBC/EG composite PCMs achieving 43.4 °C at 2.5C, compared to 72.2 °C without PCM. Youssef et al. [28] applied paraffin/EG/jute composites to a 50 Ah prismatic NMC cell, reducing temperatures from 47.27 to 36.29 °C. Fin-based systems using commercial RT42 paraffin also significantly reduced peak temperatures, such as from 84.3 to 51.1 °C at 3C [29].

Module-level studies provide greater relevance to real applications. Kong et al. [30] employed a composite PCM–liquid system in a 6S4P 21700 NMC module, limiting temperatures to 41.1 °C at 3C. Huang et al. [31] showed lower peak temperatures and improved uniformity using paraffin/EG composites in a 25P 18650 module. Ambekar et al. [32] demonstrated that tilted fin configurations enhanced uniformity in a 4S4P NMC module. In a more advanced module-level concept, Luo et al. [33] developed a pipeless cascaded BTMS combining shape-stabilized PCM channels with phase-change emulsions, reporting roughly 45-fold higher thermal conductivity than pure PCM and modest but measurable reductions in both maximum temperature and temperature non-uniformity relative to non-cascaded PCM systems.

Some studies replaced real cells with ceramic heaters to isolate heat transfer effects. Joshy et al. [34] used commercial RT35HC with ceramic heaters and found vibration increased surface temperatures. Zhang et al. [35] used 106 ceramic heaters to study hybrid PCM–liquid cooling, achieving better control than PCM alone.

Hybrid PCM–heat-pipe systems have also shown improved thermal performance. Huang et al. [36] tested pure PCM, PCM/HP–Air, and PCM/HP–Liquid in 18650 modules at 1–3C, with the PCM/HP–Liquid system reaching only 50 °C at 3C and maintaining 3 °C temperature uniformity. Chen et al. [37] showed optimal performance in a prismatic LFP module when the PCM melting point was below the heat pipe activation temperature.

Only a limited number of module-level studies have used pure PCM without additives. Hallaj and Selman [38] introduced a paraffin-based BTMS in simulation, while Hallaj et al. [39] experimentally tested 18 650 packs at up to 2.08C. Amir et al. [40] used cetyl alcohol in a 13P20S pack and reported 42.8 °C at 0.5C discharge but provided only a single cycle without ambient measurements. Patel et al. [41] applied OM35 PCM in a 12S1P 21700 module, reducing peak temperatures from 65 to 46 °C at 1C and from 90 to 53 °C at 2C.

In addition to PCM selection and system architecture, the thickness of the PCM layer has been identified as a critical design parameter

for BTMS performance. Vashisht et al. [42] experimentally studied INR18650 cells with PCM layers of 1.25, 2.50, and 5.00 mm, showing surface temperature reductions of about 10 °C at high C-rates and identifying optimal thickness ranges of roughly 2.5–3.0 mm for 1–1.5C and 2.0–2.5 mm for 2C and above, based on melt fraction and newly defined cooling metrics. John et al. [43] used 3D simulations of a stearic-acid-based BTMS with CuO nano-additives and found that a minimum PCM thickness of about 4 mm is required, with an analytically optimal thickness near 8 mm and only marginal additional temperature reduction at 12 mm. Wagh and Saha [44] numerically evaluated hybrid cooling with 1–3 mm PCM layers and internal/extended fins, demonstrating that increasing thickness from 1 to 2 mm substantially lowers peak temperatures at 3C while achieving high melt fractions, whereas a 3 mm layer is underutilized, and that fin geometry and convective heat transfer coefficients must be co-optimized with PCM thickness.

Overall, prior literature predominantly focuses on single-cell experiments, hybrid cooling, or PCM-enhanced composites. Many works employ simplified conditions, rely on numerical or heater-based emulation, or test only a single cycle. In contrast, the present study evaluates a pure-PCM BTMS using commercial RT35HC paraffin in a 3P4S module of twelve 21700 NCA cells under prolonged cycling up to 100 charge–discharge cycles at 1, 1.5, and 2C. Ambient temperature and battery-ambient differences are explicitly measured, enabling a realistic assessment of PCM effectiveness across EV-relevant SOC windows (0–100% for BEVs and 20–80% for PHEVs). From a quantitative standpoint, prior PCM-based module studies typically report peak temperatures of 40 °C–55 °C at 1–2C using pure paraffins or composite PCMs; for example, 46 °C and 53 °C at 1C and 2C with OM35 in a 12S1P 21700 module [41], or 42.8 °C at 0.5C in a 13P20S pack using cetyl alcohol [40]. Enhanced PCM systems incorporating EG fillers, metal foams, or fins typically achieve 43 °C–53 °C at 2–3C [25,27,30,36]. In the proposed configuration, the RT35HC-based PCM module limits peak module temperatures to approximately 32 °C at 1C and below 46 °C at 2C, while the associated PCM mass lowers the module gravimetric energy density from 231 $W\,h\,kg^{-1}$ to 146 $W\,h\,kg^{-1}$. Overall, this balance between thermal performance and gravimetric energy density is comparable to that achieved by more complex composite or hybrid PCM systems, but is realized here with a simpler, lower-cost, and more readily manufacturable pure-PCM design.

2. Experimental

2.1. Testing of the candidate PCMs

For BTMS, pure PCMs without additives were preferred; therefore, two fatty acids, capric acid (CA) and lauric acid (LA), each with a purity of 99% from Thermo Scientific, and two commercial paraffins, RT35 and RT35HC, procured from Rubitherm, Germany, were selected based on the prior experience by the authors [45,46]. The PCM selection explicitly accounted for both the expected operating temperatures of the cells and the ambient conditions during testing. All four materials have melting ranges within the recommended operating window of lithium-ion batteries and 20 °C ambient temperature typical for the mild northern climate in Finland, ensuring that phase change occurs in the relevant temperature range for passive, ambient-temperature thermal regulation. The melting temperature (T_m) and latent heat of fusion (ΔH_m) of the four candidate PCMs are summarized in Table 1.

To evaluate their suitability as candidate PCMs, fatty acids and commercial paraffins were characterized using Differential Scanning Calorimetry (DSC) with a DSC 204 F1 Phoenix instrument, which is regularly calibrated for temperature and enthalpy using standard reference materials. Approximately 10 mg of each sample was subjected to five consecutive heating and cooling cycles over a temperature range of 0 to 85 °C at a constant rate of 2 °C min^{-1} under a nitrogen atmosphere. The relatively wide 0 °C to 85 °C DSC range was originally selected based on initial trials that included stearic and palmitic acids, which have higher melting points of approximately 71 °C and 64 °C, respectively. Although these PCMs were later excluded from the main study, the same measurement range was retained to maintain consistency across all DSC tests. The DSC measurements provided the melting temperature, the solidification temperature and the latent heat of fusion (ΔH_m), which are critical parameters to assess the thermal performance of PCMs in BTMS applications. The measured ΔH_m values remained consistent across cycles, confirming the repeatability and reliability of the DSC data used for the estimation of the PCM mass Additionally, the specific heat capacities in the solid phases (C_S) and liquid (C_L) were also measured.

Table 1
Thermo-physical properties of the candidate PCMs.

Candidate PCMs	T_m (°C)	ΔH_m ($J\,g^{-1}$)	Source
CA	30.73	141.83	[47]
LA	42	175.8	[48]
RT35	32–38	160	[49]
RT35HC	34–36	240	[50]

2.2. Calculation of the amount of PCM needed

The amount of PCM was estimated assuming that the battery cells and the PCM should absorb all the heat generated without any heat losses to the ambient during continuous charge–discharge cycling at 2C rate for a desired time before a cooling break. The battery temperature should stay below 45 °C during this time. The irreversible and reversible heat generation are given by [51]:

$$P_{irr} = nR_{int}I^2 \tag{1}$$

$$P_{rev} = -nIT\frac{dOCV}{dT} \tag{2}$$

where n is the number of battery cells, R_{int} is the internal resistance of a single cell, I is the applied current, T is the battery temperature, and OCV is the open-circuit voltage of the cell.

Exact determination of P_{rev} would require combined $dOCV/dT$ measurements and calorimetric verification of single-cell heat generation, which is beyond the scope of this module-scale study. Instead, we rely on Ref. [51], which shows that for NCA cells the reversible (entropic) heat is generally small compared with the irreversible losses over most of the operating window, becoming significant only near the end of discharge. Calorimetric measurements shown in Electronic Supplementary information (ESI) confirm that the total heat generation peaks near the end of the discharge. However, the DC value of the internal resistance $R_{int,DC}$ is more than twice the AC value provided by the manufacturer (Table 2), introducing a much larger uncertainty in P_{irr} and the resulting PCM mass than that associated with neglecting P_{rev}. On this basis, P_{rev} is neglected in the PCM sizing calculations, and only the irreversible term is used to estimate the heat generation:

$$Q_{irr} = P_{irr}\Delta t = nR_{int}I^2\Delta t \tag{3}$$

where Δt is the time interval over which heat is generated.

This heat is absorbed by the battery cells and the PCM, respectively:

$$Q_{bat}^{sens} = n\,m_{bat}\,C_{bat}\,\Delta T \tag{4}$$

where m_{bat} is the mass of a single battery cell, C_{bat} is the specific heat capacity of the battery cell, and ΔT is the temperature rise of the battery.

$$Q_{PCM} = Q_{PCM}^{sens} + Q_{PCM}^{lat} = m_{PCM}\left(C_{PCM}\,\Delta T + f_m\,\Delta H_{PCM}\right) \tag{5}$$

where m_{PCM} is the mass of PCM, Q_{PCM}^{sens} is the sensible heat absorbed by the PCM during its temperature rise before and/or after melting, and Q_{PCM}^{lat} is the latent heat absorbed by the PCM during the solid–liquid phase change. In addition, C_{PCM} is the specific heat capacity of the PCM, assumed equal in solid and liquid phases, and ΔH_{PCM} is the

Table 2
Specifications of the NCA Li-ion battery cells [52].

Parameters	Values
Manufacturer	E-One Moli Energy Corp., Taiwan
Model	Molicell INR-21700-P45B
Capacity (Typical)	4500 mAh
Cell voltage	3.6 V (Nominal), 4.2 V (Charge), 2.5 V (Discharge)
Charge current	4.2 A(Standard), 13.5 A(Maximum)
Operating temperature	0 °C to 60 °C (Charge), −40 °C to 60 °C (Discharge)
Shape	Cylindrical
Diameter	21.55 mm (Max)
Height	70.15 mm (Max)
weight	70 g (Max)
Typical impedance, $R_{int,AC}$	7 mΩ (30% SOC)
Typical impedance, $R_{int,DC}$	15 mΩ (50% SOC)

latent heat of fusion of the PCM, while f_m is the melt fraction of the PCM that undergoes phase change during the considered time interval.

The heat to be absorbed by the PCM is:

$$Q_{PCM} = Q_{irr} - Q_{bat}^{sens} \tag{6}$$

The PCM mass can be determined by combining equations (Eqs. (3)–(6)) as follows:

$$m_{PCM} = \frac{nR_{int}I^2\Delta t - nm_{bat}C_{bat}\Delta T}{C_{PCM}\Delta T + f_m\Delta H_{PCM}} \tag{7}$$

For the PCM mass calculations presented in this work, a fully melted PCM was assumed, i.e. $f_m = 1$, corresponding to complete utilization of the latent heat during the specified 2C cycling interval.

2.3. Battery module construction

In this study, commercial 21700 NCA cells were used to construct the battery modules. Detailed specifications provided by the manufacturer are summarized in Table 2.

Two 3P4S modules (16.8 V, 13.5 Ah) were assembled, as shown in Fig. 1, with cells interconnected using nickel strips and a 4.0 mm spacing between adjacent cells, set by a 3D-printed polypropylene spacer/holder. This spacing ensured electrical insulation between cells and provided a uniform gap for PCM infiltration while maintaining a compact module layout. The 3P4S configuration was selected to achieve a representative voltage and capacity suitable for module-level thermal evaluation. The modules were housed in polypropylene enclosures measuring 13 cm × 11 cm × 11 cm. One of the modules was filled with PCM at a volume sufficient to provide effective thermal regulation across all cells, as illustrated in Fig. 1(b).

2.4. Measurement system

The 3P4S battery modules, with and without PCM, were evaluated under looped cyclic charge–discharge using a Gamry Instruments system (Reference 3000 Potentiostat with 30 k booster). The first protocol employed CCCV charging and CC discharging between 3.0 and 4.2 V per cell (5–100% SOC) at 1, 1.5, and 2C rates (BEV protocol), with a 30-min rest between charge and discharge steps. The second protocol used CC charging and discharging between 3.45 and 4.05 V per cell (20–80% SOC) at 1.5 and 2C rates for ~3 h, followed by a 45-min rest (PHEV protocol). A safety temperature limit of 50 °C was enforced via a K-type thermocouple interfaced with the potentiostat. Detailed cyclic profiles are listed in Table 3.

Temperatures were measured at multiple locations within the module, including ambient, using a HIOKI LR8531 Wireless Universal Unit and LR8450 Memory HiLogger (Fig. 2(a)), with real-time data display. Thermal imaging (Optris PI 640i IR, Germany) was used to capture spatial and temporal temperature distributions during cycling at various C-rates.

Fig. 2(a) illustrates the temperature measurement locations used in the experiments. The HIOKI LR8531 unit is equipped with ten PT100 RTD sensors, of which T_1 to T_5 were positioned centrally between the battery cells to monitor the internal module temperature, inserted through dedicated slots in the polypropylene cell spacer. The RTDs were insulated with heat-shrink tubing along their length, except for the sensing tip, to ensure electrical safety. As the distance of the T_1 to T_5 tips was about 5.8 mm from the cell surfaces, they rather measure the PCM or air temperature between the cells than the actual cell surface temperature. The maximum temperature difference between the RTDs and the cell surfaces was analyzed by measuring the single cell heat generation in an Accelerated Rate Calorimeter (ARC) and by numerical modeling of heat conduction to an RTD sensor surrounded by 4 battery cells. The details of the analysis showing maximum temperature difference of 3 °C are shown in the ESI. In the PCM module, the phase change material completely filled the space between the cell pack and the enclosure and was in direct contact with the cell surfaces. The readings from the sensors (T_1–T_5) were averaged to provide a representative mean battery module temperature, T_{bat}, as expressed in Eq. (8); in the analysis, T_{bat} is therefore used as an indicator of module temperature and for comparing configurations, rather than as a direct cell-surface temperature.

$$T_{bat} = \frac{1}{5}\sum_{i=1}^{5} T_i \tag{8}$$

T_6 and T_7 were placed within the container but outside the battery module to measure the enclosure temperature. The mean box temperature, T_{box}, was obtained by averaging these two sensor readings, as defined in Eq. (9):

$$T_{box} = \frac{1}{2}(T_6 + T_7) \tag{9}$$

The seven RTDs (T_1–T_7) were positioned up to roughly the upper third of the battery cells to monitor temperature gradients and peak temperatures, which typically occur near the cell tops during operation. The remaining three RTDs (T_8–T_{10}) were placed outside the enclosure to measure ambient conditions. Their readings were averaged to determine the overall ambient temperature, T_{amb} as calculated in Eq. (10):

$$T_{amb} = \frac{1}{3}\sum_{i=8}^{10} T_i \tag{10}$$

T_G is the safety thermocouple (Type K) integrated with the Gamry 3000 potentiostat to monitor and regulate the module temperature, preventing potential thermal runaway.

During experiments, the working and counter terminals of the 30k booster were connected to the battery module's positive and negative electrodes, respectively, while the Gamry Reference 3000 was connected to the same electrodes via its working and counter sense cables. An IR thermal camera was positioned approximately 40 cm in front of the module on a tripod to capture thermal images under different charging conditions. The schematic experimental setup is shown in Fig. 2(b).

3. Results

3.1. DSC test results of the candidate PCMs

Fig. 3(a) illustrates the melting and solidification behavior of the fatty acids and commercial paraffins. The onset and peak melting and solidification temperatures of the fatty acids indicate a clear trend: longer-chain fatty acids exhibit higher transition temperatures. Supercooling effects are also evident, with capric acid showing the highest onset supercooling, whereas RT35HC paraffin exhibits the lowest. The commercial paraffins display melting ranges of 32–38 °C for RT35 and

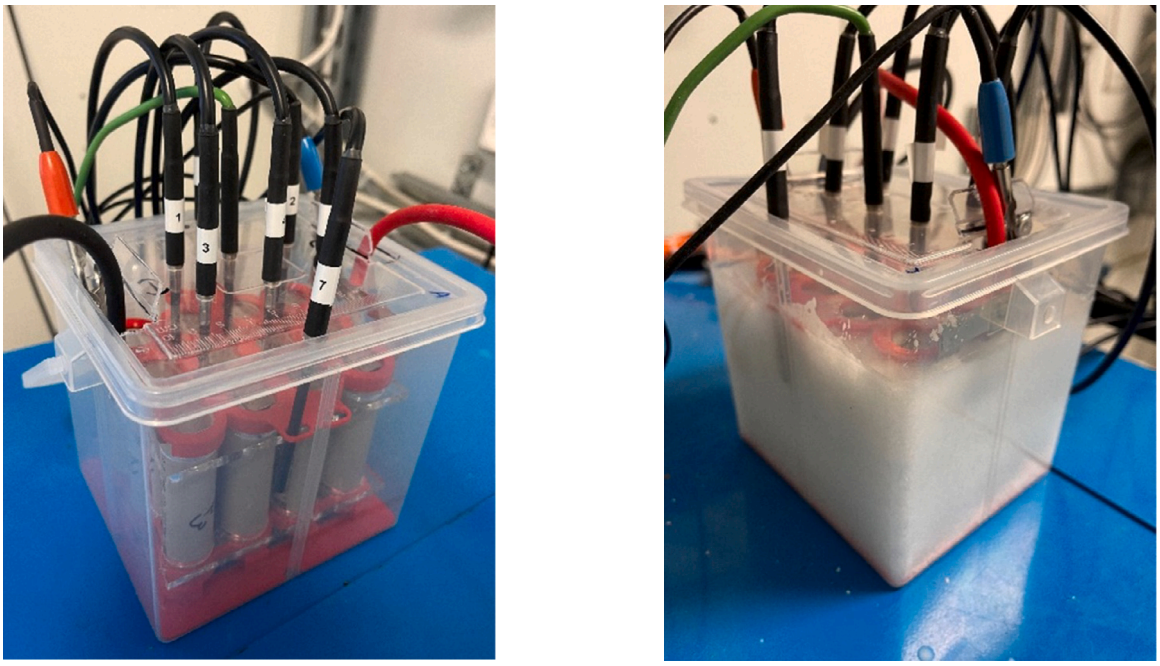

(a) (b)

Fig. 1. Photographs of the battery modules, (a) without PCM, (b) with PCM.

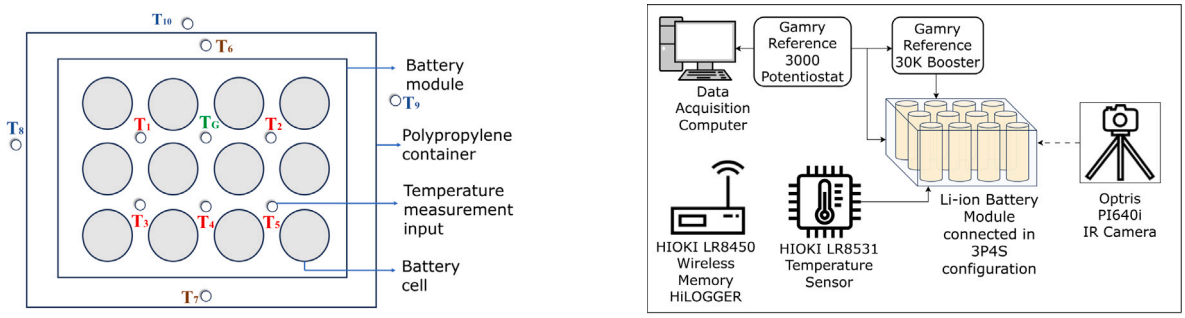

(a) (b)

Fig. 2. Schematic configuration of the, (a) Temperature measurement positions, and (b) Experimental setup for the 3P4S LIB module.

Table 3
Cycling protocols for BEV and PHEV use cases.

Parameters	BEV 1C/1.5C/2C	PHEV 1.5C/2C
Charging current	13.5 A/20.25 A/27 A	20.25 A/27 A
Charging voltage cut-off	16.8 V	16.2 V
Charge current cut-off after CV charge	150 mA	N/A
Discharge current	−13.5 A/−20.25 A/−27 A	−20.25 A/−27 A
Discharge voltage cut-off	12 V	13.8 V
Rest period	30 min between charge/discharge steps	45 min after 3 h of continuous cycling
Number of cycles tested	10/30/20	20

34–36 °C for RT35HC, with corresponding solidification ranges of 38–32 °C and 36–34 °C, respectively. These measurements are consistent with Table 1, confirming alignment with datasheet specifications.

The latent heat of fusion (ΔH_m) and solidification (ΔH_s) for the candidate PCMs are shown in Fig. 3(b). As reported in Table 1, the datasheet values of ΔH_m for RT35 and RT35HC are 160 and 240 J g^{-1}, respectively. However, DSC measurements revealed lower values than those claimed by the supplier, with RT35HC exhibiting a measured heat storage capacity corresponding to only 78% of the datasheet value. Accordingly, the PCM mass calculations in this work are based on these experimentally determined ΔH_m values (Table 4) rather than the nominal datasheet value.

Based on the DSC results (Fig. 3), RT35HC and lauric acid are identified as suitable PCM candidates for BTMS. Despite the 22% reduction in ΔH_m for RT35HC relative to the datasheet, it was selected for experimental evaluation due to its slightly lower melting temperature compared to lauric acid, good commercial availability, and practical heat absorption characteristics. The full DSC curve of RT35HC paraffin, shown in Fig. 4, exhibits multiple solidification peaks, which is typical for commercial paraffins composed of alkanes with varying chain lengths. These multiple peaks contribute to gradual heat release during

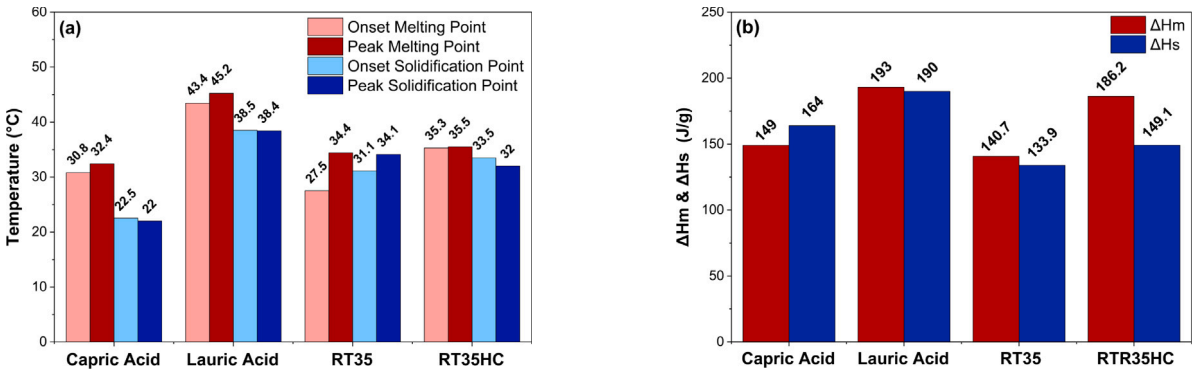

(a) (b)

Fig. 3. DSC Test results of the candidate PCMs (a) Melting and solidification points and (b) ΔH_m and ΔH_s.

Table 4
Input parameters for PCM mass calculation.

Parameter	Value	Source/Note
Internal resistance (AC) of battery, $R_{int,AC}$	0.007 Ω	Table 2
Internal resistance (DC) of battery, $R_{int,DC}$	0.015 Ω	Table 2
Internal resistance (Average) of battery, $R_{int,ave}$	0.011 Ω	Calculated average
Battery capacity, Q_{bat}^{el}	4.5 A h	Table 2
Battery mass, m_{bat}	70 g (per cell)	Table 2
Specific heat capacity of PCM, C_{pcm}	1.83 J g^{-1} K^{-1}	DSC test result
Specific heat capacity of battery, C_{bat}	0.83 J g^{-1} K^{-1}	[53]
Latent heat of PCM, ΔH_{pcm}	186 J g^{-1}	DSC test result
Temperature rise, ΔT	20 K (25–45 °C)	Assumption
Number of cells, n	12	Design specification
Time duration, Δt	3 h	Based on aggressive PHEV cycle

Table 5
Calculated PCM mass values and PCM heat capacities (heat capacities calculated using actual PCM mass).

Parameter	Value
PCM mass for $R_{int,AC}$ = 0.007 Ω, $m_{pcm,AC}$	267 g
PCM mass for $R_{int,DC}$ = 0.015 Ω, $m_{pcm,DC}$	645 g
PCM mass for $R_{int,ave}$ = 0.011 Ω, $m_{pcm,ave}$	456 g
Actual PCM mass used, $m_{pcm,act}$	490 g
Q_{bat}^{sens}	3.87 Wh
Q_{PCM}^{sens}	4.98 Wh
Q_{PCM}^{lat}	25.32 Wh

solidification, improving thermal buffering, and maintaining more uniform battery temperatures. In this context, the specific heat capacities of RT35HC paraffin were determined as 1.68 J g^{-1} K^{-1} in the solid phase (C_S) and 1.98 J g^{-1} K^{-1} in the liquid phase (C_L). By averaging these two values, the average specific heat capacity of RT35HC paraffin (C_{pcm}) can be obtained as 1.83 J g^{-1} K^{-1}, which is used in further thermal calculations.

3.2. Calculated PCM mass from the results of the DSC run

In the PCM sizing calculations based on these parameters, the melt fraction was taken as f_m = 1, i.e. the full PCM mass was assumed to undergo melting during the considered 2C cycling period, so that the entire latent heat capacity contributes to heat absorption.

Using the equations described in Section 2.2, the values relevant for the PCM mass estimation were calculated as summarized in Table 5.

The module was filled with $m_{PCM,act}$ = 490 g PCM for this study, based on the adiabatic heat-balance calculation that neglected convective and radiative heat losses. Compared with the three calculated estimates, the amount exceeds the requirement for the AC-resistance scenario, providing a margin of 223 g (+83%), and is slightly above the average-resistance estimate, with a surplus of 34 g (+7%). However, it falls short of the conservative DC-resistance case by 155 g (−24%). Because this adiabatic assumption represents a conservative worst-case (no heat dissipation to the environment), any convective and radiative heat losses during operation reduce the net heat that must be absorbed by the PCM, making the selected 490 g fill sufficient for typical 2C cycling despite the shortfall relative to the DC-resistance-based estimate.

3.3. BEV battery cycling at various C rates (1, 1.5, and 2C)

Initially, the battery module without PCM was cycled at a 1C rate for 10 cycles, with 30-min rest periods between each step. As shown in Fig. 5(b), the temperature profiles stabilized after the second cycle. The highest battery temperatures (T_{bat}) occurred at the end of the CC charging phases, reaching 37–38 °C. During subsequent CV charging phases, T_{bat} gradually decreased, reaching approximately 27 °C at the end of each 30-min rest period. The observed temperature difference between the maximum and minimum values within the module ranged from 9 to 10 °C. During CC discharging, T_{bat} increased again but remained lower than during charging, in contrast to the typical behavior of NCA cells, where heat generation during discharge can equal or exceed that during charging [51]. After each CC discharging phase, T_{bat} ranged between 33 and 35 °C, with an average peak difference of 4–5 °C between the ends of the CC charging and discharging phases. Temperature inside the polypropylene container (T_{box}) fluctuated between 30 and 31 °C during CC charging and 27–28 °C during CC discharging. Throughout the cycling test, the ambient temperature (T_{amb}) remained stable between 19.5 and 20.5 °C.

For the module with PCM (Fig. 5(d)), T_{amb} initially increased to 27.5 °C after the second cycle due to laboratory air-conditioning issues, which influenced T_{bat}, causing it to rise to approximately 34 °C. Once the ambient temperature stabilized, around 15 h later, T_{bat} reached

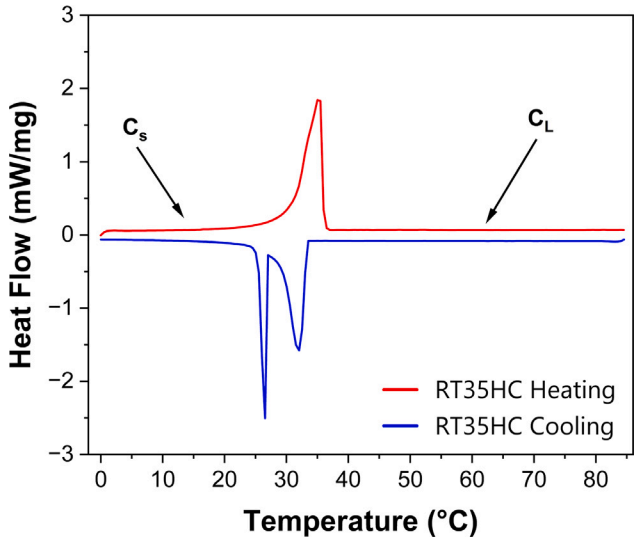

Fig. 4. DSC plot of RT35HC paraffin.

~32.2 °C at the end of CC charging and 31 °C at the end of discharging. The temperature difference between the maximum and minimum values within the module was significantly smaller than that of the non-PCM module, ranging only from 4.0 to 4.4 °C, with a 1.5 °C difference between the charging and discharging peaks. Since T_{bat} remained below the PCM melting point, these variations are primarily attributed to the sensible heat stored in the solid PCM (Q^{sens}_{PCM}). The inclusion of PCM increased the module's sensible heat storage capacity by 4.98 Wh (Table 5), which is approximately 1.3 times the heat absorbed by the battery cells, accounting for the observed reduction in temperature fluctuations.

Subsequently the battery module without PCM was cycled at a 1.5C rate for 30 cycles, as shown in Figs. 6(a) and 6(b). During the test, T_{amb} stabilized around 20 °C after the second cycle. At the end of the CC charging phases, the T_{bat} reached approximately 45 °C, while at the end of the CC discharging phases, it averaged around 40.5 °C. The minimum temperature at the end of the rest periods ranged from 32 to 33 °C. The overall temperature swing between the maximum and minimum values of the module ranged from 12 to 13 °C.

In the same test, after the 20th cycle (approximately 45 h later), T_{amb} unexpectedly increased to 23–26 °C, causing T_{bat} to exceed 47 °C (Fig. 6(b)). This triggered the potentiostat's safety sensor (T_G), halting charging and preventing the initiation of the CV charging phase. After a 30-min rest period, during which the battery cooled, cycling resumed; however, the CV charging phase was never initiated, as the battery consistently reached the temperature limit immediately following each CC charging phase. Notably, a discrepancy was observed in the potentiostat's temperature control, as the safety sensor activated at 47 °C, below the programmed set point of 50 °C. This discrepancy is attributed to the use of different sensor types: More accurate PT100 RTDs were employed for module temperature measurements (T_{bat}), whereas the Gamry safety sensor T_G is a K-type thermocouple with a different accuracy and calibration, leading to an earlier cut-off than the nominal set point.

When the PCM-filled module underwent the same cycling test (30 cycles, at 1.5C rate), the maximum T_{bat} was approximately 35 °C at the end of the CC charging phase and slightly above 34 °C after the CC discharging phase (Fig. 6(d)). The temperature difference between the peaks of the charge and discharge phases was less than 1 °C. It took roughly 9 h, or three cycles, for T_{bat} to stabilize at the maximum value. This minimal variation indicates that the PCM effectively maintained nearly constant temperatures throughout charging and discharging, demonstrating its efficiency in mitigating thermal fluctuations within the module. The minimum T_{bat} at the end of the rest period ranged from 32 to 33 °C, and the overall temperature difference between the maximum and minimum module temperatures was only 2–3 °C. As T_{box} remained below the PCM melting point, the PCM located between and immediately around the cells was sufficient to regulate the temperature, while the additional PCM in the box remained solid. This shows that the PCM thermal management is very efficient around its melting point, and the heat conductivity of the PCM is sufficient at moderate charging rates.

Since the battery module without PCM reached a peak temperature of 47 °C at the 1.5C rate, it was deemed unsafe to test higher charge and discharge rates under the same conditions. In contrast, the PCM-filled module exhibited significantly improved thermal performance, with a maximum temperature of only ~35 °C at 1.5C. Consequently, the 2C cycling test was conducted solely on the PCM module to evaluate its thermal behavior under higher charge rates, performed over 20 cycles as shown in Fig. 7.

At 2C rate, the PCM-filled battery module reached a peak temperature of approximately 42 °C at the end of each CC charging phase and ~41 °C at the end of each CC discharging phase. The minimum T_{bat} at the end of rest periods averaged 34 °C, resulting in a temperature variation of 7–8 °C. During the 20-cycle test (Fig. 7(b)), T_{bat} exceeded the PCM's melting range (31–35 °C), reducing its heat-regulating effectiveness and leading to a wider temperature swing of 7 °C. It took roughly 7 h, or three cycles, for T_{bat} to stabilize, while T_{box} required nearly 11 h to reach 35 °C, reflecting the time needed for the melting front to propagate to the RTDs. At the end of the rest periods, temperatures remained above the lower limit of the PCM melting range, indicating only partial solidification and limiting the PCM's heat absorption capacity. This diminished thermal control at higher charge/discharge rates may adversely affect battery performance and lifespan.

3.3.1. IR thermal images of the battery modules in different conditions

IR thermal images were captured at the end of the CC charging phase, when the battery module reached its peak temperature, under various cycling conditions. The boxed area in each image highlights the region occupied by the batteries within the plastic enclosure, where the highest temperatures were consistently observed in the central region, as identified using the Optris PIX Connect software. This region is critical for assessing thermal behavior and understanding temperature distribution patterns influenced by the presence or absence of PCM. While the RTDs were positioned at the top of the module, the thermal images provided a more comprehensive view of the temperature profile across the entire module.

Figs. 8(a) and 8(b) show the thermal images from the 1C cycling tests, with maximum temperatures of 40.1 °C without PCM and 34.2 °C with PCM. In both cases, the temperature difference between the middle and the top or bottom of the battery pack ranged from 2.0 to 2.5 °C. In the absence of PCM, the hotspot was located near the top of the module, reflecting a vertical heat gradient likely driven by upward convective heat flow and limited thermal regulation. In contrast, the presence of PCM redistributed heat more uniformly, shifting the hotspot toward the vertical center of the pack and indicating improved thermal homogenization.

Figs. 8(c) and 8(d) present thermal images from the 1.5C cycling tests. The maximum temperature reached 43.9 °C without PCM and 35.3 °C with PCM, with temperature variations between the middle and top or bottom again ranging from 2.0 to 2.5 °C. Similar to the 1C results, the hotspot was at the top of the module in the absence of PCM, whereas the PCM-filled module exhibited a more centralized thermal peak, demonstrating that PCM not only lowers the overall temperature rise but also mitigates vertical thermal gradients.

Fig. 8(e) shows the IR thermal image from the 2C cycling test at the end of the CC charging phase for the PCM-filled module. The maximum module temperature reached 43.8 °C. Despite the higher current rate, the thermal image still displayed a centralized hotspot, underscoring

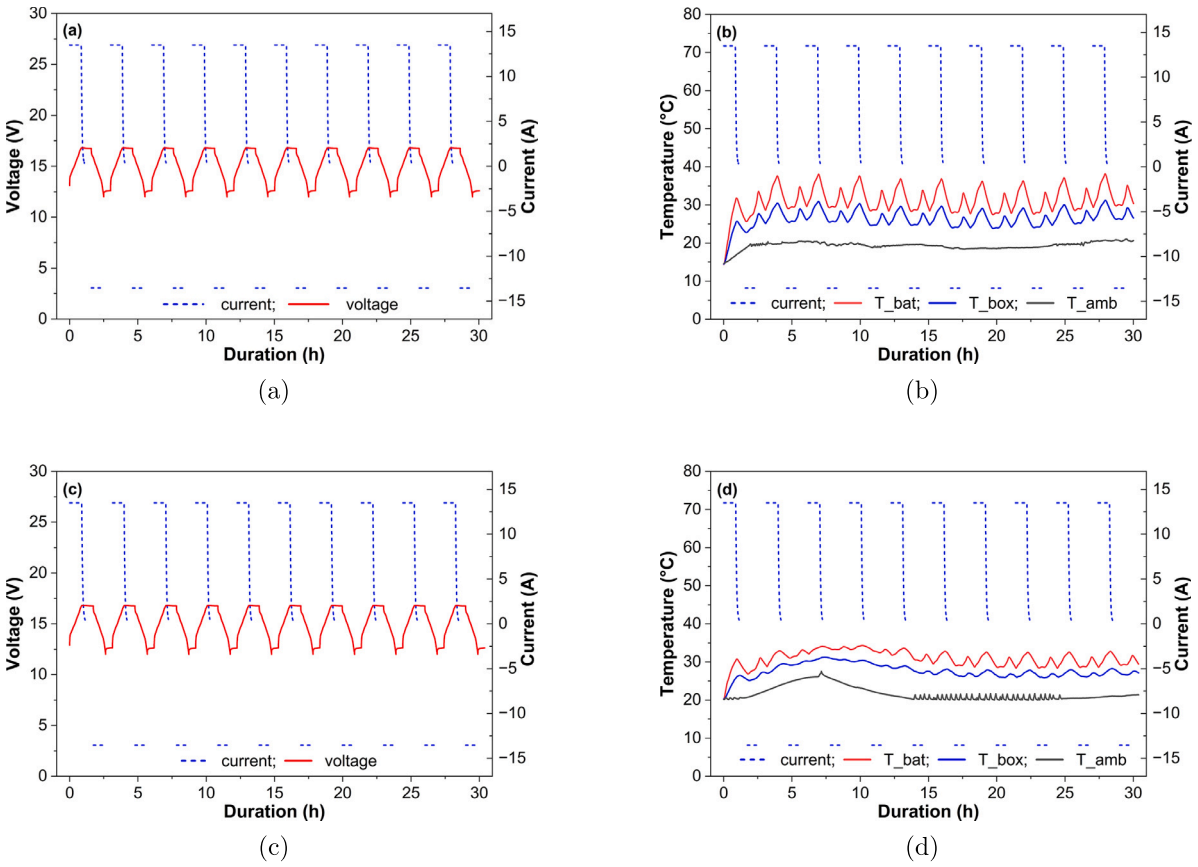

Fig. 5. Electrical and thermal profiles during 1C charge–discharge. (a) Current vs. module voltage without PCM. (b) Current vs. temperatures without PCM. (c) Current vs. module voltage with PCM. (d) Current vs. temperatures with PCM.

the PCM's effectiveness in absorbing and redistributing heat even under elevated thermal loads.

Overall, the IR images complement the RTD measurements by revealing spatial temperature distributions and hotspot locations under different cycling conditions. However, because the IR camera views the module through the transparent plastic enclosure, the measured values represent the apparent temperature of the enclosure surface rather than the true battery cell temperature. As a result, the absolute IR temperatures may deviate from actual cell surface temperatures, and the IR data are used primarily in a qualitative manner to assess relative temperature patterns and hotspots, while the RTD measurements serve as the quantitative reference for the module temperature.

3.3.2. Temperature differences inside the modules and between the batteries and the ambient

In this section, we analyze the difference between the maximum battery temperature and the ambient temperature for modules with and without PCM to evaluate the effectiveness of PCM in thermal management. As described earlier, five RTDs (T_1–T_5) were positioned inside the battery module, with T_4 centrally located in the lower row of cells (Fig. 2(a)), where heat accumulation is highest. Accordingly, T_4 was used to represent the maximum PCM or Air temperature. In contrast, T_5 consistently recorded the lowest temperature throughout the tests. The average temperature difference between T_4 and T_5 ranged from 0.9 to 1.8 °C across different cycling protocols, indicating a generally homogeneous temperature distribution within the module, as illustrated in Fig. 9(a).

Fig. 9(b) presents the temperature difference relative to ambient during the 1C cycling tests. According to the heat-transfer analysis presented in the ESI, the PCM temperature at the T_{bat} RTD locations stays at most 1.5 °C lower than the corresponding cell surface temperature during the 1C test. After the CC charging phase, the temperature difference stabilized at just over 13 °C for the PCM-filled module, compared to nearly 19 °C for the module without PCM, reflecting a 6 °C reduction attributable to PCM integration. Moreover, the temperature swing decreased from 9 °C (without PCM) to 5 °C (with PCM), demonstrating improved thermal uniformity and a lower average battery temperature when PCM was employed.

Fig. 9(c) presents the corresponding temperature profiles for the 1.5C cycling rate. The average temperature difference between the maximum battery temperature and the ambient stabilized at 17 °C for the PCM-filled module, compared to approximately 26 °C for the module without PCM, representing a substantial 9 °C reduction. The temperature swing was also significantly reduced, from 11 °C without PCM to 5 °C with PCM, confirming enhanced thermal stability within the PCM's melting range of 31–35 °C.

Since the 2C test was conducted only on the PCM-filled module, Fig. 9(d) presents the corresponding temperature difference exclusively for this configuration. The average temperature difference between the maximum battery temperature and ambient was approximately 23 °C, which is still lower than the 26 °C observed for the non-PCM module at 1.5C. During the 2C test, the PCM temperature at the T_{bat} RTD locations remains less than 3 °C below the corresponding cell surface temperature (see ESI for details). These results indicate that while the PCM continued to contribute to thermal regulation, its effectiveness was reduced at higher charge rates as temperatures exceeded the PCM's optimal melting range.

3.4. PHEV battery cycling at various C rates (1.5, and 2C)

Fig. 10 depicts the results of the 20-cycle tests for the battery modules with and without PCM at a 1.5C rate. Both experiments followed an

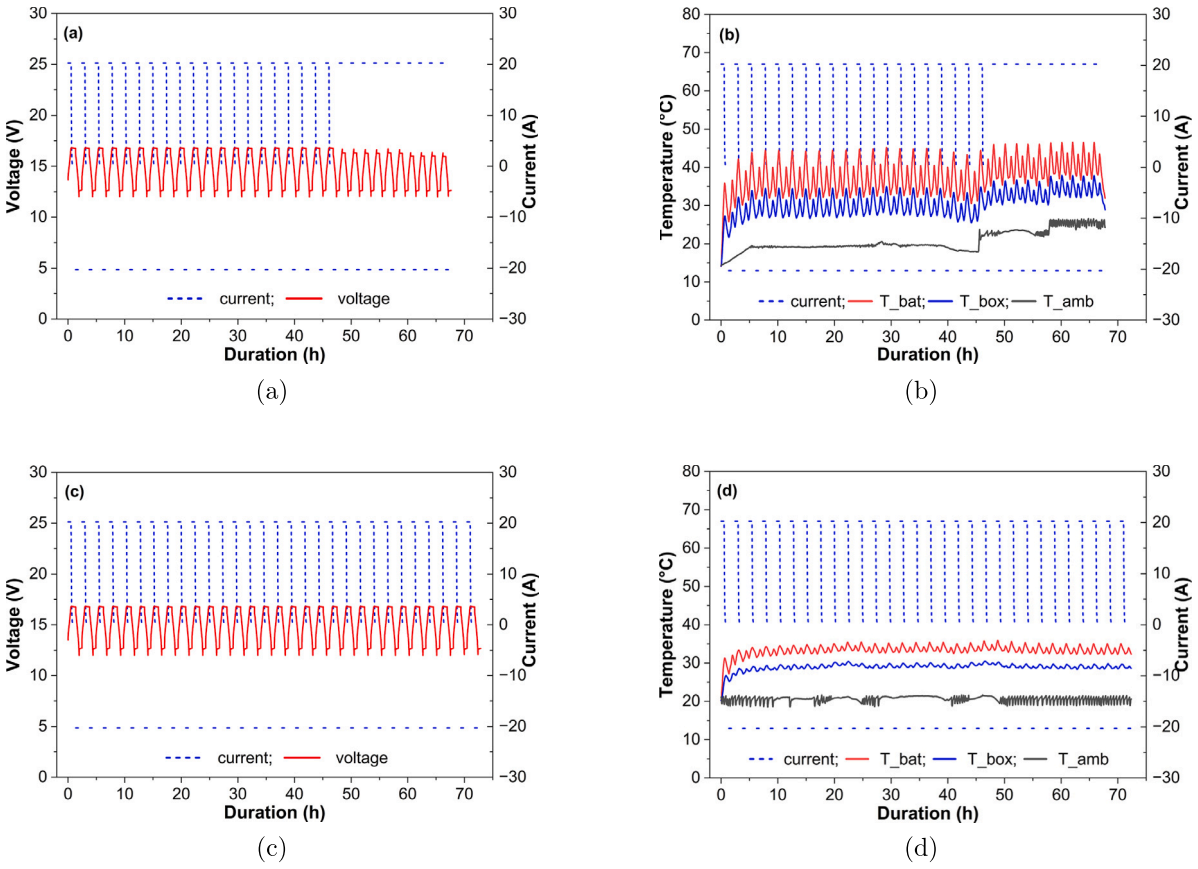

Fig. 6. Electrical and thermal profiles during 1.5C charge–discharge. (a) Current vs. module voltage without PCM. (b) Current vs. temperatures without PCM. (c) Current vs. module voltage with PCM. (d) Current vs. temperatures with PCM.

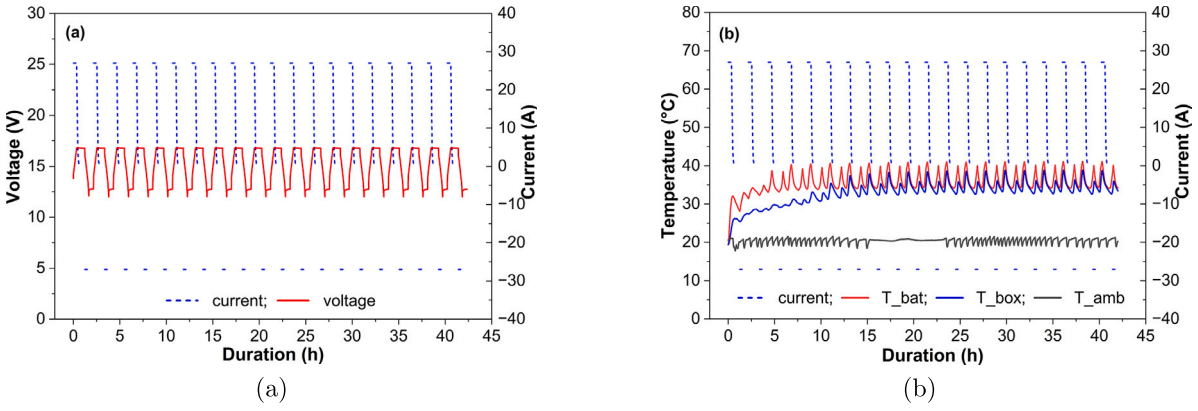

Fig. 7. Electrical and thermal profiles during 2C charge–discharge. (a) Current vs. module voltage with PCM. (b) Current vs. temperatures with PCM.

identical cycling profile, consisting of six consecutive charge–discharge cycles followed by a 45-min rest period. Each set of six cycles required approximately 3 h, resulting in a total test duration of roughly 76–77 h.

For the module without PCM, T_{bat} peaked at ~47.5 °C (Fig. 10(a)), whereas the PCM-filled module exhibited a lower peak of 38.5 °C (Fig. 10(b)). The maximum temperature recorded by T_4 was 48.1 °C in the non-PCM module and 39.1 °C in the PCM module. The enclosure temperature (T_{box}) reached 36 °C without PCM and 36.7 °C with PCM. In the PCM module, it took nearly 15 h, or three cycles, for both T_{bat} and T_{box} to stabilize.

In both configurations, the temperature increased incrementally after each charge–discharge cycle, producing six distinct peaks. However, the maximum temperature difference between the battery and ambient was higher in the non-PCM module, reaching 27.0 °C, compared to 19.8 °C in the PCM module. Notably, the PCM's melting front gradually propagated from the material surrounding the cells toward the outer regions of the module enclosure, indicating progressive utilization of the PCM's latent heat capacity.

The 2C cycling test was conducted only for the PCM-filled module (Fig. 11), as the peak temperature of the 1.5C test without PCM reached 48.1 °C. The cycling protocol consisted of eight consecutive charge–discharge cycles followed by a 45-min rest period. Each set of eight cycles required approximately 2 h and 42 min, resulting in a total test duration of ~69 h. During the experiment, T_{bat} peaked at ~45.4 °C, while T_4 recorded a maximum of 46.3 °C. T_{box} reached a maximum of 42.7 °C. It took nearly 25 h, or six cycles, for both T_{bat} and T_{box} to stabilize. Following each charge–discharge cycle, the

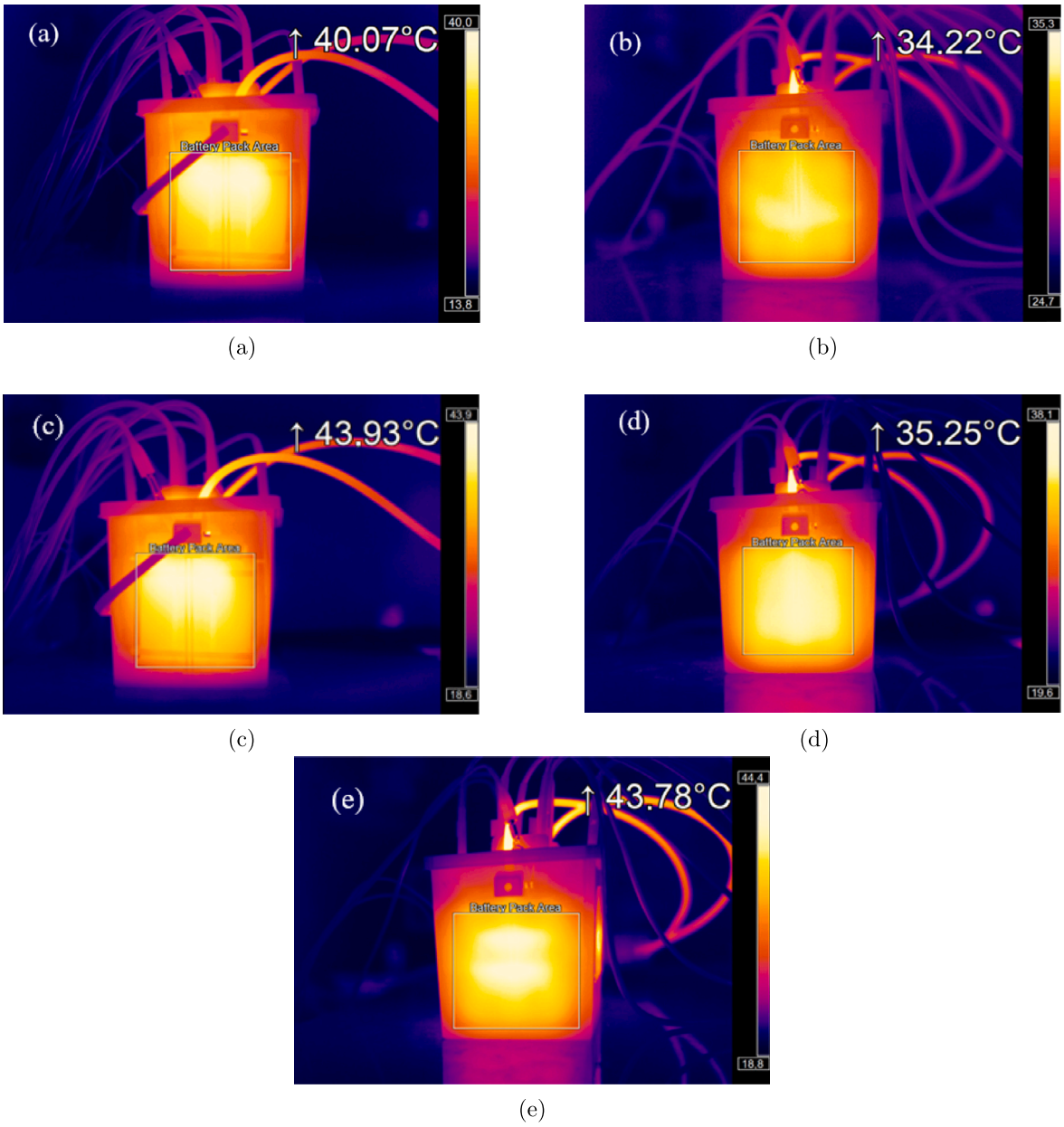

Fig. 8. IR Thermal Image of the battery module at the end of CC charging (a) at 1C rate without PCM. (b) at 1C rate with PCM. (c) at 1.5C rate without PCM. (d) at 1.5C rate with PCM. (e) at 2C rate with PCM.

T_{bat} increased incrementally, producing eight distinct peaks over the entire experiment. The temperature difference between the maximum battery temperature and ambient fluctuated, reaching a maximum of 26.9 °C, almost identical to the non-PCM module at 1.5C. Fig. 12 shows the melted PCM after the test, indicating that the temperature was sufficient to induce near-complete solid to liquid transition.

4. Discussion

The results demonstrate the performance of paraffin wax PCM in passive thermal management of a Li-ion battery module comprising 12 high-power cylindrical NCA cells over 100 charge–discharge cycles, a level of prolonged module cycling not previously reported. Various C-rates from 1C to 2C and two distinct load profiles were employed, and the results were compared with a similar module without PCM.

These findings confirm that the selection of an appropriate PCM melting point is a key design criterion for effective thermal management. In the 1C experiment, the module temperature with PCM remained below the PCM's melting point. The lower module temperature (32 vs. 38 °C) can be attributed to the sensible heat of the solid PCM, which more than doubles the effective heat capacity of the battery cells compared to the module without PCM (Table 5). The effectiveness of the PCM's latent heat was first observed at 1.5C, where the non-PCM module reached temperatures near the 50 °C safety cut-off. The PCM module reached the melting point, with peak temperatures fluctuating within a narrow interval around this value. At 2C, operation of the non-PCM module was unsafe, while the PCM module experienced near-complete melting of the PCM, resulting in a larger temperature swing above the melting point. Nevertheless, PCM effectively delayed temperature rise, keeping the peak module temperature below 46 °C even under aggressive PHEV cycling conditions. Testing at higher C-rates was limited by the potentiostat and booster. The remaining solid PCM (Fig. 12) suggests that improving thermal conductivity could further exploit the full cooling potential of the PCM.

Temperature differences in the air gaps between battery cells remained around 2 °C and were slightly lower in the PCM filled gaps.

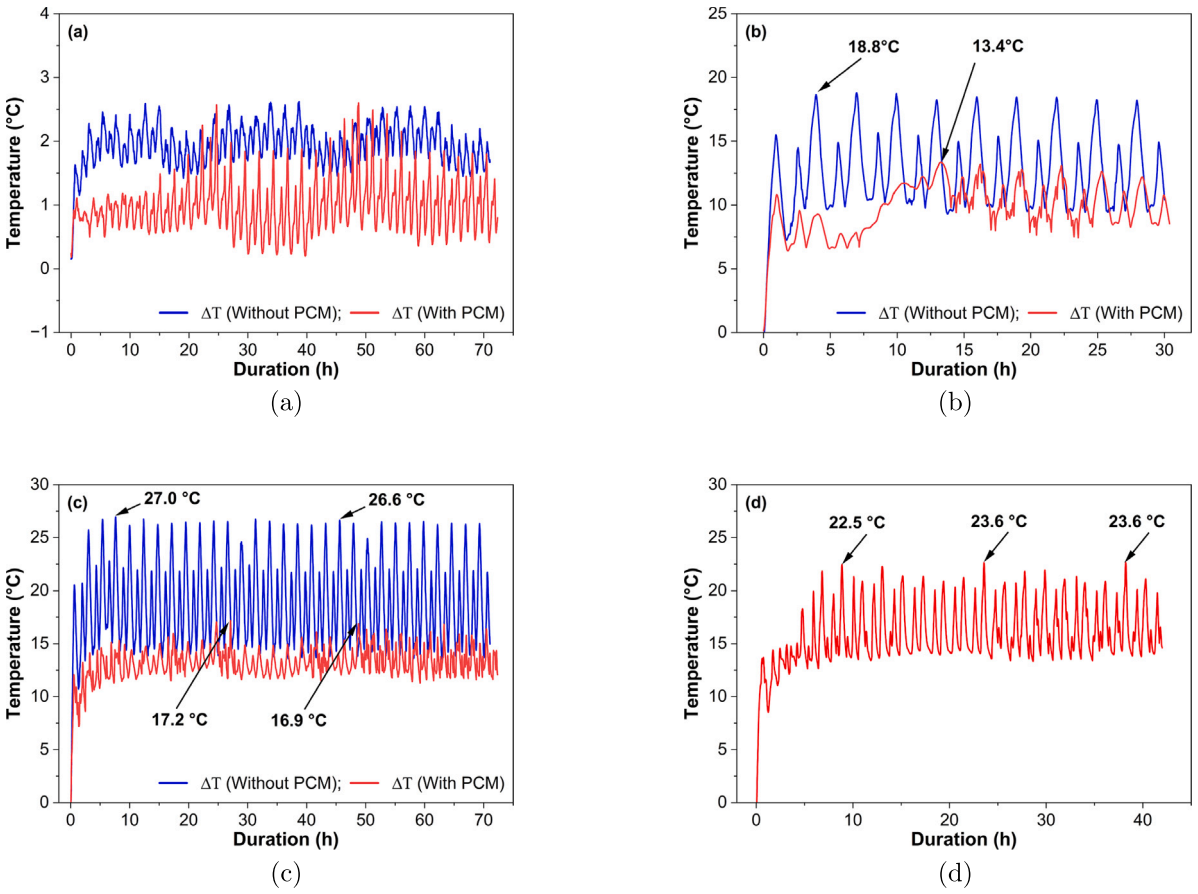

Fig. 9. (a) Difference between the maximum and minimum temperature within the module with and without PCM for 1.5C rate test. Temperature difference of the module's maximum and ambient temperatures with and without PCM (b) at 1C rate. (c) at 1.5C rate. (d) at 2C rate.

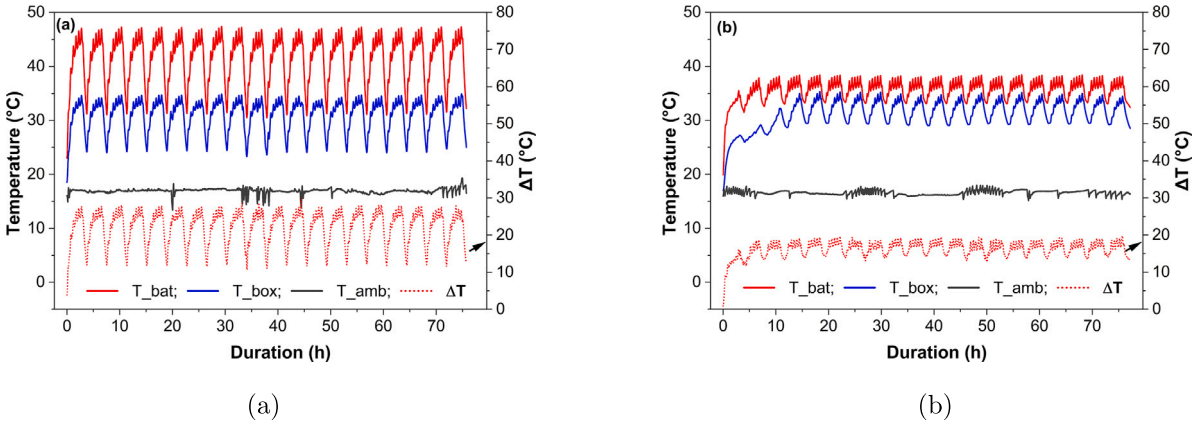

Fig. 10. Temperature profile for the 20-cycle test at 1.5C rate, (a) without PCM and (b) with PCM.

Based on the ARC measurements and numerical modeling shown in the ESI, the cells surface temperature is estimated to be maximum 1.5 and 3 °C above the measured PCM temperature at 1C, and 2C, respectively. Direct measurement of the cell surface temperature is recommended for any further work. IR images (Fig. 8) indicate a vertical temperature gradient in the non-PCM module, which was partially mitigated in the PCM module; the IR thermography is therefore used to identify major non-uniformities, although small internal hotspots cannot be fully excluded. These results suggest that PCM reduces peak module temperatures and improves thermal uniformity, potentially enhancing battery life and reducing the need for cell balancing.

The heat capacity calculations in Table 5 provide a straightforward method for estimating the PCM quantity required for operation at a given C-rate. For the present module, a PCM mass of 490 g was selected by matching the heat that can be absorbed through the measured latent heat ΔH_m of RT35HC to the estimated irreversible heat generation at a 2C discharge under an adiabatic (no convective or radiative losses) assumption, rather than through a formal multi-objective optimization. This sizing leads to a PCM-to-battery mass ratio that reduces the gravimetric energy density of the module from 231 $W\,h\,kg^{-1}$ (without PCM) to 146 $W\,h\,kg^{-1}$ (with PCM), which remains competitive with liquid-cooled systems in small-scale applications. However, reversible heat generation in other Li-ion chemistries introduces uncertainties in

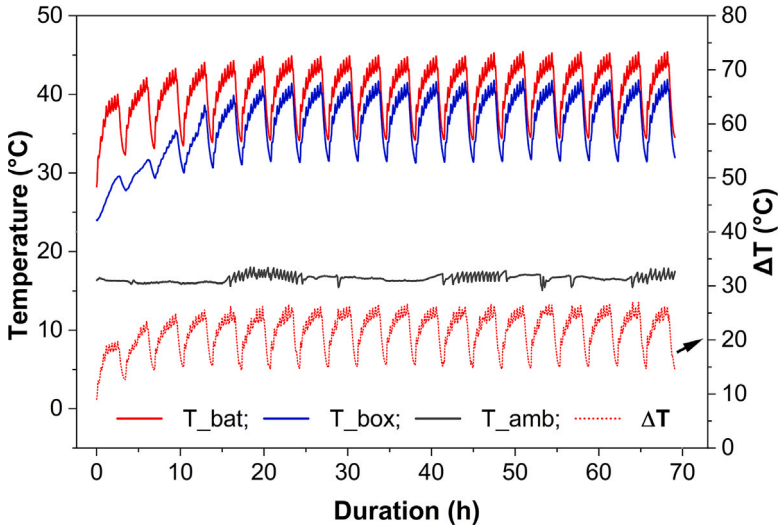

Fig. 11. Temperature profile for the 20-cycle test at 2C rate with PCM module.

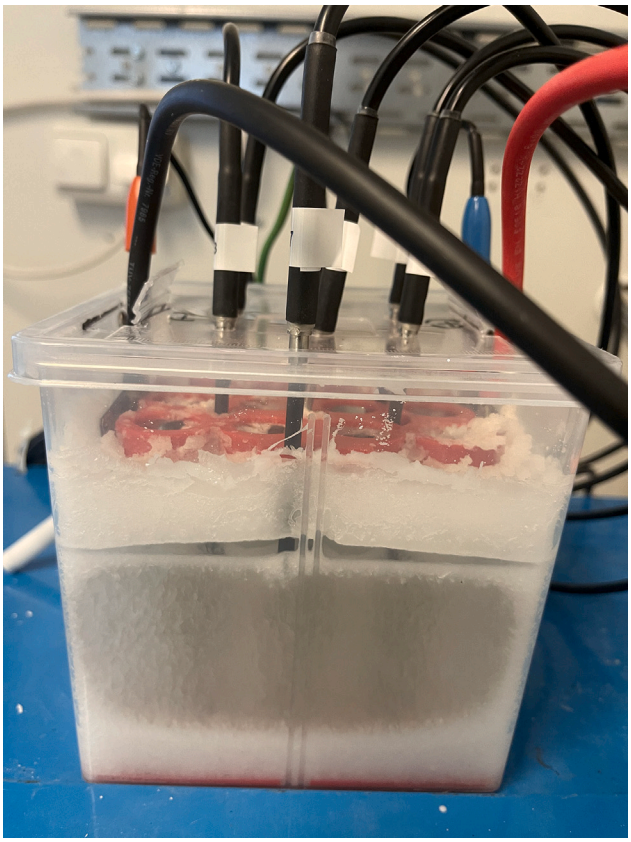

Fig. 12. Molten PCM inside the battery box after the 2C cycling experiment.

predicting actual cooling requirements [51]. Thermal characterization of single cells before module design is recommended to improve the design and estimate the actual PCM need more accurately.

Differences in PCM temperature between cells and at the module edges reflect the propagation of the melting front. These results indicate that the PCM's thermal conductivity is sufficient for intermediate cycling rates, but enhancement would be beneficial at cycling rates above 1.5C. A numerical electrochemical–thermal model would enable more detailed thermal analysis [54], although developing such a model requires in-depth knowledge of single-cell behavior and internal structure, which is beyond the scope of this study. Additionally, our modules exhibited lower heat generation during discharge than during charge, contrary to previous reports for NCA cells [51,54]. The ARC measurement shown in the ESI confirms lower average heat generation of a single cell during discharge than during charge. These results deserve more detailed analysis in the future.

DSC measurements revealed that the heat of fusion for commercial paraffin wax is considerably lower than the datasheet value, emphasizing the importance of verifying the performance of PCM prior to application and implementing rigorous quality control to ensure long-term reliability.

Lauric acid (LA) could serve as an alternative PCM, exhibiting slightly higher heat of fusion (193 $J\,g^{-1}$) and significantly higher melting point (43 °C) compared to RT35HC paraffin. However, industrial-grade fatty acids often contain impurities that reduce heat of fusion and may alter the melting point. The lower melting point of RT35HC is advantageous for battery durability under moderate charging rates, whereas a higher melting point could enhance thermal protection under high-rate charging above 2C.

Nonetheless, addressing the potential safety risks associated with PCM use in commercial applications is critical. Organic PCMs, including paraffin-based materials and fatty acids, are inherently flammable and may exacerbate thermal runaway in the event of system failure. Future research should focus on incorporating flame-retardant additives or developing non-flammable PCM alternatives that maintain high thermal storage capacity and stability. In addition, optimizing packaging design to efficiently contain phase transitions and prevent leakage could further enhance the safety and practical applicability of PCM-based battery thermal management systems.

5. Conclusion

This study demonstrates the effectiveness of passive thermal management of a small Li-ion battery module using commercial paraffin wax PCM without additives. Comparison with a similar module without PCM shows that at low C-rate (1C), the sensible heat of the PCM is sufficient to limit the temperature rise of the battery. At intermediate C-rate (1.5C), where the module reaches the melting point of the PCM, the battery exhibits a reduced temperature swing, as the phase change process moderates both heating and cooling rates. At high C-rate (2C), nearly the full latent heat capacity of the PCM is exploited, and although the temperature continues to rise, the PCM significantly delays this increase. In the present study, the module without PCM could be safely operated only up to 1.5C, whereas the PCM-filled module could

be operated safely up to 2C. The study further underlines that the battery temperature should be measured directly at the cell surfaces due to the poor heat conductivity of the organic PCM materials, and conductive additives are recommended for high charge and discharge rates above 1.5C.

A simple heat balance calculation, assuming negligible heat loss to the ambient, was successfully employed to estimate the required amount of PCM. However, neglecting reversible heating effects may not be appropriate for other Li-ion chemistries beyond NCA. To gain a more detailed understanding of module-level thermal performance, development of a numerical electrochemical–thermal model for individual cells within modules would be necessary. The results provide new insights into the design of passive BTMS for small scale NRMM, and can be used for verification of more complex design tools.

CRediT authorship contribution statement

Arijeet Paul Avik: Writing – original draft, Visualization, Validation, Investigation, Formal analysis, Data curation. **Arunachala Mada Kannan:** Writing – review & editing, Supervision, Methodology, Conceptualization. **Vesa Ruuskanen:** Resources, Methodology. **Soroush Mostafaie:** Software, Formal analysis. **Pertti Kauranen:** Writing – review & editing, Supervision, Resources, Project administration, Methodology, Investigation, Funding acquisition, Conceptualization.

Declaration of competing interest

The authors declare that they have no known competing financial interests or personal relationships that could have appeared to influence the work reported in this paper.

Acknowledgments

The authors express their gratitude to the Kymenlaakso Higher Education Society for funding this research under the Energy Storage Professorship at LUT University. A part of the study was carried out under the Flexible Clean Propulsion Technologies project (ref. 10063/31/2023), which is co-funded by Business Finland. Turku University of Applied Sciences is acknowledged for the ARC measurements and Mr. Muhammad Sarwar for the heat transfer modeling.

Appendix A. Supplementary data

Supplementary material related to this article can be found online at https://doi.org/10.1016/j.applthermaleng.2025.129563.

Data availability

Data will be made available on request.

References

[1] Z. Li, Y. Zhang, S. Zhang, B. Tang, Phase change materials for lithium-ion battery thermal management systems: A review, J. Energy Storage 80 (2024) 110259, http://dx.doi.org/10.1016/j.est.2023.110259.

[2] T. Sasaki, Y. Ukyo, P. Novák, Memory effect in a lithium-ion battery, Nat. Mater. 12 (2013) 569–575, http://dx.doi.org/10.1038/nmat3623.

[3] J. Pesonen, R. Prinz, H. Ovaskainen, P. Kauranen, A. Poikela, K. Kärhä, Alternative powertrains and fuels in heavy non-road mobile machinery and their future expectations - A review, Curr. For. Rep. 11 (2025) http://dx.doi.org/10.1007/s40725-024-00244-2.

[4] M.S. Houache, C.H. Yim, Z. Karkar, Y. Abu-Lebdeh, On the current and future outlook of battery chemistries for electric vehicles—Mini review, Batteries 8 (2022) 70, http://dx.doi.org/10.3390/batteries8070070.

[5] S. Saptakee, Powering the Future of Nickel with NMC 811 Batteries, Tech. Rep., Carbon Credits, 2024, URL https://carboncredits.com/powering-the-future-of-nickel-with-nmc-811-batteries-aemc/.

[6] Y. Miao, P. Hynan, A.V. Jouanne, A. Yokochi, Current Li-ion battery technologies in electric vehicles and opportunities for advancements, Energies 12 (2019) 1074, http://dx.doi.org/10.3390/en12061074.

[7] Y. Ding, Z.P. Cano, A. Yu, J. Lu, Z. Chen, Automotive Li-ion batteries: Current status and future perspectives, Electrochem. Energy Rev. 2 (2019) 1–28, http://dx.doi.org/10.1007/s41918-018-0022-z.

[8] G. Zeng, Z. Bai, P. Huang, Q. Wang, Thermal safety study of Li-ion batteries under limited overcharge abuse based on coupled electrochemical-thermal model, Int. J. Energy Res. 44 (2020) 3607–3625, http://dx.doi.org/10.1002/er.5125.

[9] J. Weng, Q. Huang, X. Li, G. Zhang, D. Ouyang, M. Chen, A.C.Y. Yuen, A. Li, E.W.M. Lee, W. Yang, J. Wang, X. Yang, Safety issue on PCM-based battery thermal management: Material thermal stability and system hazard mitigation, Energy Storage Mater. 53 (2022) 580–612, http://dx.doi.org/10.1016/j.ensm.2022.09.007.

[10] L. Ianniciello, P.H. Biwolé, P. Achard, Electric vehicles batteries thermal management systems employing phase change materials, J. Power Sources 378 (2018) 383–403, http://dx.doi.org/10.1016/j.jpowsour.2017.12.071.

[11] D. Aurbach, Y. Talyosef, B. Markovsky, E. Markevich, E. Zinigrad, L. Asraf, J.S. Gnanaraj, H.J. Kim, Design of electrolyte solutions for Li and Li-ion batteries: A review, Electrochim. Acta 50 (2004) 247–254, http://dx.doi.org/10.1016/j.electacta.2004.01.090.

[12] S. Cai, X. Zhang, J. Ji, Recent advances in phase change materials-based battery thermal management systems for electric vehicles, J. Energy Storage 72 (2023) 108750, http://dx.doi.org/10.1016/j.est.2023.108750.

[13] Y. Zhao, B. Zou, T. Zhang, Z. Jiang, J. Ding, Y. Ding, A comprehensive review of composite phase change material based thermal management system for lithium-ion batteries, Renew. Sustain. Energy Rev. 167 (2022) 112667, http://dx.doi.org/10.1016/j.rser.2022.112667.

[14] V. Zinth, C.V. Lüders, M. Hofmann, J. Hattendorff, I. Buchberger, S. Erhard, J. Rebelo-Kornmeier, A. Jossen, R. Gilles, Lithium plating in lithium-ion batteries at sub-ambient temperatures investigated by in situ neutron diffraction, J. Power Sources 271 (2014) 152–159, http://dx.doi.org/10.1016/j.jpowsour.2014.07.168.

[15] A. Wazeer, A. Das, C. Abeykoon, A. Sinha, A. Karmakar, Phase change materials for battery thermal management of electric and hybrid vehicles: A review, Energy Nexus 7 (2022) 100131, http://dx.doi.org/10.1016/j.nexus.2022.100131.

[16] C. Liu, D. Xu, J. Weng, S. Zhou, W. Li, Y. Wan, S. Jiang, D. Zhou, J. Wang, Q. Huang, Phase change materials application in battery thermal management system: A review, Materials 13 (2020) 1–37, http://dx.doi.org/10.3390/ma13204622.

[17] M. Koniak, A. Czerepicki, Selection of the battery pack parameters for an electric vehicle based on performance requirements, in: IOP Conference Series: Materials Science and Engineering, vol. 211, Institute of Physics Publishing, 2017, http://dx.doi.org/10.1088/1757-899X/211/1/012005.

[18] Z. Wang, X. Li, G. Zhang, Y. Lv, C. Wang, F. He, C. Yang, C. Yang, Thermal management investigation for lithium-ion battery module with different phase change materials, RSC Adv. 7 (2017) 42909–42918, http://dx.doi.org/10.1039/c7ra08181b.

[19] S.K. Maknikar, A.M. Pawar, Application of phase change material (PCM) in battery thermal management system (BTMS): A critical review, Mater. Today: Proc. (2023) http://dx.doi.org/10.1016/j.matpr.2023.08.329.

[20] L. Yang, J. nan Huang, F. Zhou, Thermophysical properties and applications of nano-enhanced PCMs: An update review, Energy Convers. Manage. 214 (2020) 112876, http://dx.doi.org/10.1016/j.enconman.2020.112876.

[21] M. Zhi, R. Fan, X. Yang, L. Zheng, S. Yue, Q. Liu, Y. He, Recent research progress on phase change materials for thermal management of lithium-ion batteries, J. Energy Storage 45 (2022) 103694, http://dx.doi.org/10.1016/j.est.2021.103694.

[22] Z. Rao, S. Wang, G. Zhang, Simulation and experiment of thermal energy management with phase change material for ageing LiFePO4 power battery, Energy Convers. Manage. 52 (2011) 3408–3414, http://dx.doi.org/10.1016/j.enconman.2011.07.009.

[23] J. Weng, X. Yang, G. Zhang, D. Ouyang, M. Chen, J. Wang, Optimization of the detailed factors in a phase-change-material module for battery thermal management, Int. J. Heat Mass Transfer 138 (2019) 126–134, http://dx.doi.org/10.1016/j.ijheatmasstransfer.2019.04.050.

[24] G. Srivastava, R. Nandan, M.K. Das, Thermal runaway management of Li ion battery using PCM: A parametric study, Energy Convers. Manag.: X 16 (2022) 100306, http://dx.doi.org/10.1016/j.ecmx.2022.100306.

[25] A.R. Bais, D.G. Subhedar, S. Panchal, Critical thickness of nano-enhanced RT-42 paraffin based battery thermal management system for electric vehicles: A numerical study, J. Energy Storage 52 (2022) 104757, http://dx.doi.org/10.1016/j.est.2022.104757.

[26] J.T. Rajan, V.S. Jayapal, M.J. Krishna, K.A.M. Firose, S. Vaisakh, A.K. John, A. Suryan, Analysis of battery thermal management system for electric vehicles using 1- tetradecanol phase change material, Sustain. Energy Technol. Assess. 51 (2022) 101943, http://dx.doi.org/10.1016/j.seta.2021.101943.

[27] W. Wu, J. Liu, M. Liu, Z. Rao, H. Deng, Q. Wang, X. Qi, S. Wang, An innovative battery thermal management with thermally induced flexible phase change material, Energy Convers. Manage. 221 (2020) 113145, http://dx.doi.org/10.1016/j.enconman.2020.113145.

[28] R. Youssef, M.S. Hosen, J. He, M. Al-Saadi, J.V. Mierlo, M. Berecibar, Novel design optimization for passive cooling PCM assisted battery thermal management system in electric vehicles, Case Stud. Therm. Eng. 32 (2022) 101896, http://dx.doi.org/10.1016/j.csite.2022.101896.

[29] V.G. Choudhari, A.S. Dhoble, S. Panchal, Numerical analysis of different fin structures in phase change material module for battery thermal management system and its optimization, Int. J. Heat Mass Transfer 163 (2020) 120434, http://dx.doi.org/10.1016/j.ijheatmasstransfer.2020.120434.

[30] D. Kong, R. Peng, P. Ping, J. Du, G. Chen, J. Wen, A novel battery thermal management system coupling with PCM and optimized controllable liquid cooling for different ambient temperatures, Energy Convers. Manage. 204 (2020) 112280, http://dx.doi.org/10.1016/j.enconman.2019.112280.

[31] R. Huang, Z. Li, W. Hong, Q. Wu, X. Yu, Experimental and numerical study of PCM thermophysical parameters on lithium-ion battery thermal management, Energy Rep. 6 (2020) 8–19, http://dx.doi.org/10.1016/j.egyr.2019.09.060.

[32] S. Ambekar, P. Rath, A. Bhattacharya, A novel PCM and TCE based thermal management of battery module, Therm. Sci. Eng. Prog. 29 (2022) 101196, http://dx.doi.org/10.1016/j.tsep.2022.101196.

[33] J. Luo, H. Gu, X. Xu, L. Huang, D. Zou, Development of a pipeless, cascade phase change power battery thermal management system, J. Clean. Prod. 423 (2023) 138797, http://dx.doi.org/10.1016/j.jclepro.2023.138797.

[34] N. Joshy, M. Hajiyan, A.R.M. Siddique, S. Tasnim, H. Simha, S. Mahmud, Experimental investigation of the effect of vibration on phase change material (PCM) based battery thermal management system, J. Power Sources 450 (2020) 227717, http://dx.doi.org/10.1016/j.jpowsour.2020.227717.

[35] H. Zhang, X. Wu, Q. Wu, S. Xu, Experimental investigation of thermal performance of large-sized battery module using hybrid PCM and bottom liquid cooling configuration, Appl. Therm. Eng. 159 (2019) 113968, http://dx.doi.org/10.1016/j.applthermaleng.2019.113968.

[36] Q. Huang, X. Li, G. Zhang, J. Zhang, F. He, Y. Li, Experimental investigation of the thermal performance of heat pipe assisted phase change material for battery thermal management system, Appl. Therm. Eng. 141 (2018) 1092–1100, http://dx.doi.org/10.1016/j.applthermaleng.2018.06.048.

[37] K. Chen, J. Hou, M. Song, S. Wang, W. Wu, Y. Zhang, Design of battery thermal management system based on phase change material and heat pipe, Appl. Therm. Eng. 188 (2021) 116665, http://dx.doi.org/10.1016/j.applthermaleng.2021.116665.

[38] S.A. Hallaj, J.R. Selman, A novel thermal management system for electric vehicle batteries using phase-change material, J. Electrochem. Soc. 147 (2000) 3231, http://dx.doi.org/10.1149/1.1393888.

[39] S. Al-Hallaj, R. Kizilel, A. Lateef, R. Sabbah, M. Farid, J. Selman, Passive thermal management using phase change material (PCM) for EV and HEV Li-ion batteries, in: 2005 IEEE Vehicle Power and Propulsion Conference, 2005, pp. 376–380, http://dx.doi.org/10.1109/VPPC.2005.1554585.

[40] M. Amir, A. Sadar, N. Mohammad, Enhancing electric vehicle battery pack performance: A PCM-based study on battery thermal management in the energy market, IEEE J. Emerg. Sel. Top. Ind. Electron. (2024) 1–8, http://dx.doi.org/10.1109/JESTIE.2024.3462827.

[41] J. Patel, R. Patel, R. Saxena, A. Nair, Experimental investigation of thermal characteristics of a 12S1P Li-ion NMC-21700 battery module under different environments for EV applications, Int. J. Thermofluids 26 (2025) 101084, http://dx.doi.org/10.1016/j.ijft.2025.101084.

[42] S. Vashisht, D. Rakshit, Unravelling the impact of PCM thickness: Passive thermal management for INR18650 Li-ion cells across discharge rates, Therm. Sci. Eng. Prog. 53 (2024) 102758, http://dx.doi.org/10.1016/j.tsep.2024.102758.

[43] S. John, K. Sreyas, Y. Mohan, A.D. Thampi, S. Rani, Numerical investigation on the effect of PCM thickness and nano-additive on the cooling performance of stearic acid based battery thermal management system, in: Materials Today: Proceedings, vol. 80, Elsevier Ltd, 2023, pp. 1442–1447, http://dx.doi.org/10.1016/j.matpr.2023.01.267.

[44] V.A. Wagh, S.K. Saha, Optimising extended fin design and heat transfer coefficient for improved heat transfer and PCM recover time in thermal management of batteries, Appl. Therm. Eng. 255 (2024) 123964, http://dx.doi.org/10.1016/j.applthermaleng.2024.123964.

[45] P. Kauranen, K. Peippo, P. Lund, An organic PCM storage system with adjustable melting temperature, Sol. Energy 46 (1991) 275–278, http://dx.doi.org/10.1016/0038-092X(91)90094-D.

[46] P. Kauranen, L. Wikström, J. Heikkinen, J. Laurikko, T. Elonen, A. Seppälä, Lämpö- ja Kylmäakut Kuljetusvälineissä: Loppuraportti, Tech. Rep. VTT-R-02312-09, VTT Technical Research Centre of Finland, Tampere, Finland, 2010, p. 92, URL https://publications.vtt.fi/julkaisut/muut/2010/VTT-R-02312-09.pdf.

[47] W. Du, H. Fei, Q. He, L. Wang, Y. Pan, J. Liu, Preparation and properties of capric acid-stearic acid-based ternary phase change materials, RSC Adv. 11 (2021) 24938–24948, http://dx.doi.org/10.1039/d1ra03925c.

[48] P. Zhao, Q. Yue, H. He, B. Gao, Y. Wang, Q. Li, Study on phase diagram of fatty acids mixtures to determine eutectic temperatures and the corresponding mixing proportions, Appl. Energy 115 (2014) 483–490, http://dx.doi.org/10.1016/j.apenergy.2013.10.048.

[49] RT35 PCM: Product Data Sheet. https://www.rubitherm.eu/media/products/datasheets/Techdata_-RT35_EN_18042024.PDF.

[50] RT35HC PCM: Product Data Sheet. https://www.rubitherm.eu/media/products/datasheets/Techdata_-RT35HC_EN_09102020.PDF.

[51] Y. Yuan, Q. Ma, X. Zhang, F. Zhang, X. Song, H. Xin, G. Zhu, H. Zhang, Influence of cathode materials on thermal characteristics of lithium-ion batteries, Front. Chem. 12 (2024) 1324840, http://dx.doi.org/10.3389/fchem.2024.1324840.

[52] Molicel INR-21700-P45B: Product Data Sheet. https://www.molicel.com/wp-content/uploads/INR21700P45B_1.2_Product-Data-Sheet-of-INR-21700-P45B-80109.pdf.

[53] K.A. Murashko, J. Pyrhönen, J. Jokiniemi, Determination of the through-plane thermal conductivity and specific heat capacity of a Li-ion cylindrical cell, Int. J. Heat Mass Transfer 162 (2020) 120330, http://dx.doi.org/10.1016/j.ijheatmasstransfer.2020.120330.

[54] F. Bahiraei, A. Fartaj, G.A. Nazri, Electrochemical-thermal modeling to evaluate active thermal management of a lithium-ion battery module, Electrochim. Acta 254 (2017) 59–71, http://dx.doi.org/10.1016/j.electacta.2017.09.084.